Quantum trapping and rotational self-alignment in triangular Casimir microcavities

PHYSICS

Quantum trapping and rotational self-alignment in triangular Casimir microcavities

Betül Küçüköz[1]†, Oleg V. Kotov[1]†, Adriana Canales[1]†, Alexander Yu. Polyakov[1], Abhay V. Agrawal[1], Tomasz J. Antosiewicz[1,2], Timur O. Shegai[1]*

Casimir torque, a rotational motion driven by zero-point energy minimization, is a problem that attracts notable research interest. Recently, it has been realized using liquid crystal phases and natural anisotropic substrates. However, for natural materials, substantial torque occurs only at van der Waals distances of ~10 nm. Here, we use Casimir self-assembly with triangular gold nanostructures for rotational self-alignment at truly Casimir distances (100 to 200 nm separation). The interplay of repulsive electrostatic and attractive Casimir potentials forms a stable quantum trap, giving rise to a tunable Fabry-Pérot microcavity. This cavity self-aligns both laterally and rotationally to maximize area overlap between templated and floating flakes. The rotational self-alignment is sensitive to the equilibrium distance between the two triangles and their area, offering possibilities for active control via electrostatic screening manipulation. Our self-assembled Casimir microcavities present a versatile and tunable platform for nanophotonic, polaritonic, and optomechanical applications.

INTRODUCTION

The quantum nature of van der Waals forces was initially revealed by London (*1*) and subsequently generalized by Casimir and Polder (*2*). Furthermore, Casimir (*3*) extended this concept to describe the attraction between two ideal mirrors, which brought a quantum electrodynamics effect to the macroscopic scale. Following this, Lifshitz and co-authors (*4*, *5*) developed a theory that allowed for the calculation of the Casimir effect between arbitrary planar mirrors, relying on the classical optical response of materials. This advancement paved the way for predicting both repulsive (*6*, *7*) and lateral Casimir forces (*8*–*10*) in various contexts.

The introduction of asymmetry allows extending the Casimir effect to a new degree of freedom, rotation. In this respect, Casimir torque led by quantum fluctuations was first predicted by Kats (*11*) and Parsegian and Weiss (*12*) when considering dielectric media with in-plane anisotropy at short separation distances. Later, the approach was generalized to longer distances by Barash (*13*). However, the predicted torque was small and turned out to be challenging to observe. The first Casimir torque measurements were reported only recently (*14*, *15*). In these measurements, a solid isotropic interlayer was used, which helped support two anisotropic materials at a fixed distance and in a parallel configuration. The torque was measured by optical characterization of the twist of a liquid crystal, which acted as one of the birefringent bodies. Such a setup allowed controlling the sign and strength of the torque by choosing an anisotropic substrate material and varying the interlayer thickness but did not allow to observe the torque directly, since the rotation was hidden inside the liquid crystal. Furthermore, the torque between two media with artificial in-plane anisotropy, such as lamellar gratings, was predicted to be substantially greater than in natural anisotropic materials (*16*, *17*). In particular, Guérout *et al.* (*16*) obtained the torque per unit area for the infinite gratings and accounted for the finite-size effects using the overlap area approximation, which works well when the lateral size of the gratings is much larger than their characteristic length scales and the gap between them. Recently, Antezza *et al.* (*17*) calculated the Casimir torque between finite-sized metallic gratings beyond the overlap approximation. It turned out that a finite number of gratings periods leads to not only oscillations of the torque direction but also a much larger magnitude of the torque than intuitively expected. Moreover, because of a critical zero-order geometric transition between a two-dimensional (2D) and a 1D periodic system, the torque per unit area can reach extremely large values, increasing without bounds with the size of the system, which paves the way to observation of the torques at truly Casimir distances ~100 nm and beyond.

An alternative way to observe Casimir torques is offered by the optical levitation of anisotropic dielectric nanoparticles (silica in particular) in vacuum (*18*–*20*). This method has ultrahigh sensitivity but requires high vacuum conditions and works only with relatively small nanoparticles that can be captured using conventional optical tweezers. Therefore, this method does not allow direct imaging of the Casimir torque in an optical microscope but instead relies on polarization-dependent readout.

We note that the aforementioned works primarily focus on Casimir interactions in dry or vacuum environments. However, the introduction of liquids can be beneficial; in particular, repulsive Casimir forces have been successfully demonstrated using a combination of high refractive index liquid bromobenzene interfaced between two solids, gold and glass substrates (*6*), as well as in gold-ethanol-teflon systems (*21*). Furthermore, the liquid environment allows to use colloids as a platform for studying Casimir interactions. The theoretical framework for describing colloidal interactions in solution is often based on the DLVO theory, which typically involves electrostatic stabilization to balance attractive van der Waals forces (*22*, *23*). Recently, the DLVO theory has been extended to account for retardation effects (*24*, *25*).

Van der Waals and Casimir interactions in colloidal solutions play an important role not only in their stability but also in self-assembly (*21*, *26*–*31*). Recently, the formation of self-assembled, stable Fabry-Pérot (FP) cavities has been achieved through a combination of attractive Casimir and repulsive electrostatic interactions (*25*). This

[1]Department of Physics, Chalmers University of Technology, 412 96 Gothenburg, Sweden. [2]Faculty of Physics, University of Warsaw, Pasteura 5, 02-093 Warsaw, Poland.
*Corresponding author. Email: timurs@chalmers.se
†These authors contributed equally to this work.

development opens up possibilities for strong light-matter interactions and highlights the intrinsic relationship between the original Casimir problem and the planar microcavity problem. Moreover, the electrostatic force in the system can be actively modified, enabling the tuning of the FP resonance within a certain range without compromising cavity stability. The repulsive electrostatic force in the Casimir microcavity can be controlled by adjusting the ion concentration of the aqueous solution. This delicate balance between the attractive Casimir force and the repulsive electrostatic force not only stabilizes the FP cavity in the vertical direction but also enables the formation of laterally stable structures.

The Casimir self-assembly approach offers numerous advantages, but it also presents certain challenges. These challenges include slow diffusion-limited cavity formation, irreproducibility, unscalable fabrication, and a lack of integration with microfluidics. One potential solution to address these challenges is the use of templated structures. Substrates that are templated with various nanostructured patterns are commonly used in self-assembled colloidal systems and plasmonic arrays (*32*–*35*). Implementing this approach could help overcome several problematic issues on the road toward realizing asymmetry-induced Casimir torques in liquid environments and scalable and stable formation of Casimir microcavities in vertical, horizontal, and rotational domains. However, to date, the templated self-assembly approach has not been explored for Casimir self-assembly and Casimir torques.

Here, we introduce template-assisted systems for the self-assembly of Casimir microcavities, where patterned metallic surfaces on the substrate are crucial for achieving lateral Casimir forces and self-alignment through Casimir torque. We specifically chose an equilateral triangle geometry to realize the Casimir torque, as triangles' symmetry provides the highest possible torque among other equilateral microstructures. We investigate the self-alignment of triangular nanoflakes in an aqueous solution at room temperature by monitoring the rotational motion induced by the lateral Casimir force, which strives to maximize the overlap area between the top colloidal flake and the bottom templated flake on the substrate. This rotational effect is substantial and can be observed in real time using an optical microscope. In addition, we study the influence of thermal fluctuations, the separation distance between the flakes, and their areas on the stability of the obtained microcavities. Our approach not only enables the scalability of the Casimir self-assembly and self-alignment but also paves the way for the integration of Casimir torque effects with colloidal science, nanophotonics, polaritonics, and self-assembly. On a broader account, it is important to mention that Casimir and Casimir torque effects studied here could be relevant for the design of microelectromechanical devices (*36*) and in future devices relying on an efficient and contactless transfer of angular momentum (*37*–*40*).

RESULTS AND DISCUSSION

The process of formation of stable Casimir microcavities in aqueous solution (*25*) can be substantially enhanced and more accurately controlled by combining top-down nanopatterned gold areas (referred to as "seeds") on the glass substrate and floating Au flakes in the solution (Fig. 1A). This approach allows to control the density, size, and shape of the seeds, which is unavailable for the previous method. Over time, the floating Au flakes, playing the role of "micromirrors," diffuse toward the seeds and form dimers due to lateral Casimir forces. Moreover, if the seeds are triangular, the floating flakes not only form stable cavities but also geometrically align with the seeds to maximize the overlap area (and hence minimize the Casimir potential; see Fig. 1C).

In this work, we focus specifically on equilateral triangles (Fig. 1A). Experiments are designed with two main components: (i) glass substrates with the precisely fabricated seeds produced by electron beam lithography and (ii) single crystal Au flakes in aqueous solution produced by wet chemical synthesis (*41*). Triangular Au seeds with lateral dimensions in the 4 to 10 μm range and 20 nm heights are shown in Fig. 1D (also see Methods). The seed approach allows us to control the Casimir force on the floating Au flake. Since it is difficult to control the colloidal growth with high precision (*41*), chemically synthesized Au flakes are typically obtained in a range of sizes, thicknesses, and shapes. To simplify the self-alignment problem, we therefore preselect only equilateral triangle flakes of appropriate size by dragging them with optical tweezers to the seeds.

Stable dimers emerge as a result of the equilibrium between two opposing forces, the attractive Casimir force and the repulsive electrostatic force, occurring at a specific distance denoted as L_{eq}. Furthermore, these dimers support optical FP resonances that can be modified by controlling L_{eq}. This is illustrated in Fig. 1E, where variations in the reflected light's color are depicted for different L_{eq} values. The corresponding reflection spectra, as shown in Fig. 1F, serve as the basis for the experimental determination of L_{eq} (see Methods). The variation of L_{eq} not only affects the FP resonance but also substantially influences the Casimir potential, which scales approximately as $L_{eq}^{-2.6}$ for 30-nm-thick Au flakes (*25*). The manipulation of L_{eq} can be achieved by adjusting the total ion concentration in the solution, due to altering the Debye-Hückel screening length of electrostatic repulsion, described by κ^{-1} (see Methods, Eq. 4). Furthermore, the engineering of geometric patterns on the substrate allows to use diverse sizes of triangular Au seeds and flakes (Fig. 1D). This approach facilitates an investigation into the influence of overlap areas on the lateral Casimir force (Fig. 1B).

A specific example of Casimir self-alignment, depicted in Fig. 1G, demonstrates the nearly isolated nature of two distinct motions: lateral and rotational (movie S3), enabling their separate analysis. Throughout the self-assembly and self-alignment process, the floating Au flake initially exhibits predominantly lateral motion, moving toward the Au seed with minimal rotation. This lateral shift aims to increase the overlap area. Subsequently, in the second phase, the floating flake begins to rotate, ultimately achieving full overlap with the seed. It is intriguing to observe the individual contributions of these two motions to the overall increase in the overlap area and eventually forming a stable dimer (see movies S1 to S3).

In what follows, we analyze both, the dimer formation process and the stability of the self-assembled dimers to thermal fluctuations. Furthermore, by using the seed concept, the system's behavior can be controlled by both L_{eq} and the total area of the Au seeds. The forthcoming sections provide a detailed exploration of how both of these parameters affect the Casimir potential, the dimer formation, the self-alignment process, and the robustness of these alignments to thermal fluctuations.

Accelerated dimer formation by lateral and rotational Casimir forces

Previously, we elucidated the advantages of using the seed approach for achieving lateral motion and enhancing stability in lateral alignment with the corresponding seed. In this section, we additionally note that the lateral motion of the flake exhibits varying speeds during

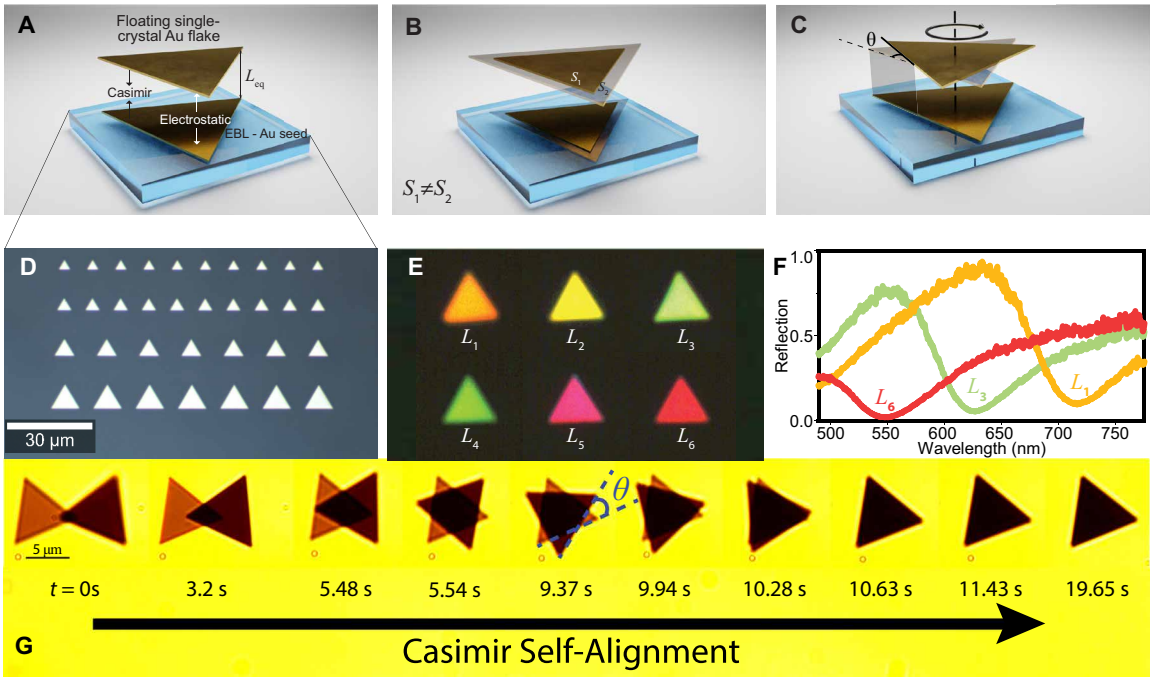

Fig. 1. Self-assembled triangular Casimir microcavities composed through a combination of top-down lithography and colloidal chemistry. (**A**) Schematic illustration of the triangular seed approach on the glass substrate and Casimir self-assembly forming a stable Fabry-Pérot (FP) microcavity. (**B**) The seed approach allows exploring the effect of overlap area on Casimir self-alignment and its stability to thermal fluctuations. (**C**) Illustration of the rotation angle (θ) variation as the flakes self-align. The angle θ is defined as the angle between the edges of the seed and the floating flake. When the floating flake is fully aligned to the seed θ = 0. (**D**) Optical bright-field image of the templated Au seed arrays on a glass substrate with a = 4, 5, 7, and 10 μm edge lengths, respectively. (**E**) True-color reflectivity images of self-aligned Casimir microcavities using 5-μm seeds recorded at distinct L_{eq} values, denoted as L_i for i = 1,2, …,6. (**F**) Reflection spectra of the self-aligned FP microcavities used to determine L_{eq} by the transfer-matrix method. $L_1 > L_3 > L_6$, i.e., L_1 = 199, L_3 = 161, and L_6 = 123 nm, respectively. (**G**) Selected video frames of the self-alignment process. The floating flake initially approaches the seed in the opposite orientation and begins rotating around t = 9.37 s. The rotation continues until the flakes are fully aligned, after which the configuration remains stable.

the dimer formation with the seed. This phenomenon is especially evident when the floating flake approaches the seed with the same orientation. The lateral Casimir force draws the floating flake toward the Au seed, which causes a concurrent increase in the overlap area between the flake and the seed, $S(t)$. When the initial orientations of the triangles match, dimer formation occurs without any rotational motion, simplifying the observation of lateral motion acceleration and alterations in acceleration with increasing overlap area. This process is evidenced in Fig. 2. Initially, when the overlap area is minimal, the flake's motion is slow and of predominantly Brownian nature. Over time, the seed exerts a robust attraction on the floating flake, eventually leading to full area overlap, S_0. The lateral and rotational motions stop when the two triangles achieve perfect overlap and alignment. Our data analysis involves extracting the overlap area of the seed and Au flake from each frame of the videos (movies S1 and S2) and normalizing it with the total area of the seed (or floating flake), $S(t)/S_0$, as depicted in Fig. 2A.

Since the separation distance is intricately linked to the Casimir potential, the acceleration of the Au flake exhibits a direct dependence on L_{eq}. This is demonstrated in Fig. 2A, where we present $S(t)/S_0$ for two distinct L_{eq} values. It is important to highlight the critical role played by L_{eq}, given its strong influence on the lateral Casimir forces; even slight alterations in L_{eq} yield a substantial impact on the acceleration dynamics of the Au flake. The inset pictures correspond to video frames depicting the exemplary data points. Furthermore, we calculate the position changes over time by tracing the displacement of the center of mass of the floating flake with respect to that of the seed, $x(t)$.

Because of the viscous friction in the liquid and the small mass of the flake, the motion under the lateral Casimir force in our case occurs deeply in the overdamped regime ($\Gamma_x >> \omega_x$, where Γ_x is the oscillator's lateral damping constant normalized to the mass and ω_x is the oscillator's eigen frequency). In this regime, the role of the flake's mass is negligible, and the general solution of the equation of motion (see Supplementary Theory and figs. S4 and S5) can be reduced to the sum of the fast $e^{-\Gamma_x t}$ (microsecond scale) and slow $-e^{\omega_x^2/\Gamma_x t}$ (second scale) decaying exponents with a negligible role of the former. Then, on a time scale of seconds, the lateral (and rotational) motion obeys the slow decaying exponential function $x(t) = \tilde{a}[1 - e^{\tilde{\omega}(t-t_{max})}]$, where $\tilde{\omega} = \omega_x^2/\Gamma_x$ is a characteristic effective frequency and $\tilde{a}$ is close to the triangle's edge size a as long as $t_{max} >> \tilde{\omega}^{-1}$ (see Supplementary Theory). Notably, the nonharmonic nature of the lateral overlap potential results in the inverse curvature of this exponential function, while in a harmonic case, the decaying solution exhibits an ordinary positive curvature $x(t) \sim ae^{-\tilde{\omega}t}$. The effective frequency $\tilde{\omega} = |U_0| D_x \sqrt{3}/2k_B T$ ~1 Hz is determined by the total potential per unit area U_0 (with Casimir and electrostatic contributions) and the lateral diffusion coefficient D_x. These contributions distinctly depend on L_{eq}. Specifically, the absolute value of the total potential grows with a decrease in L_{eq} as follows: $|U_0| \sim |Ae^{-\kappa L_{eq}} - BL_{eq}^{-\alpha}|$, where A and B

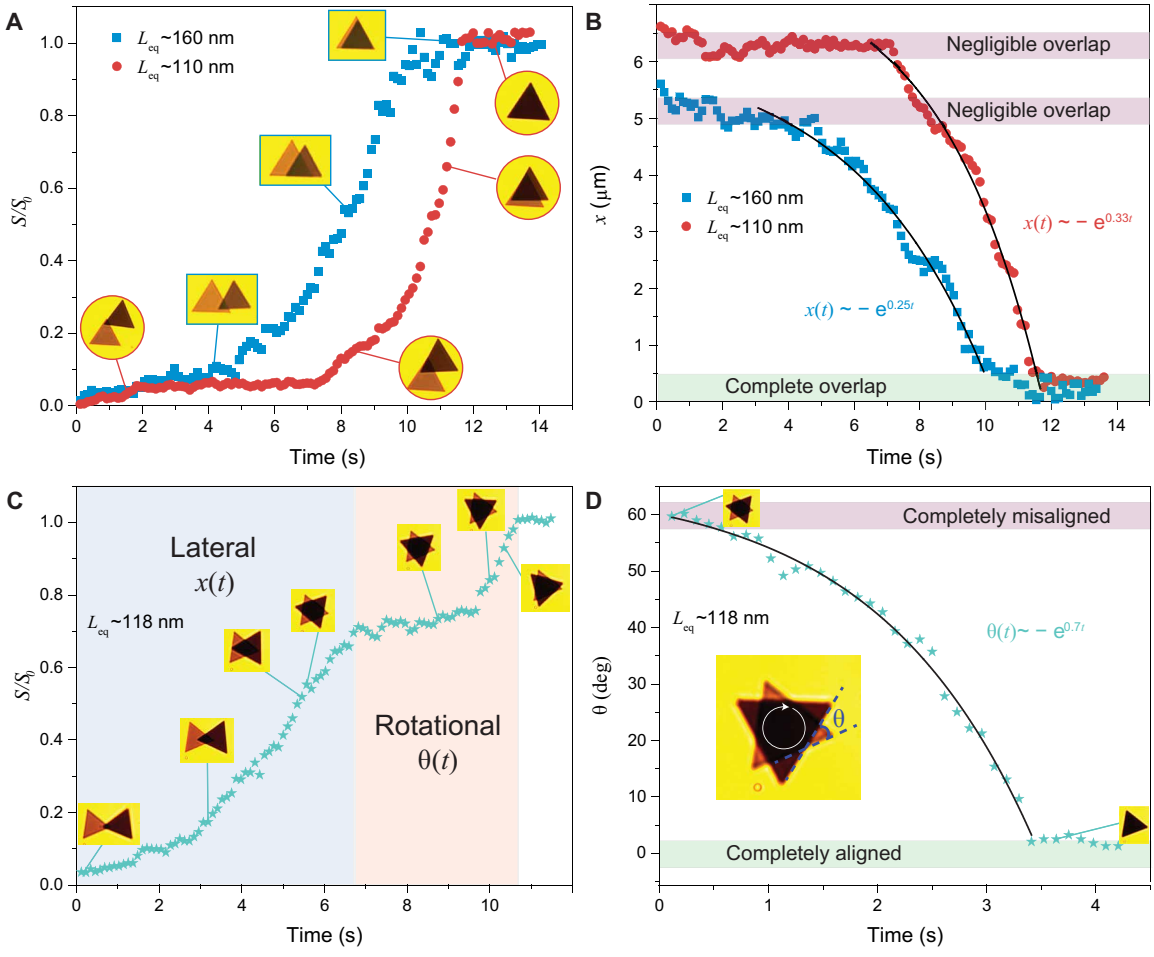

Fig. 2. Formation of stable Casimir microcavities along lateral (*x*) and rotational (θ) coordinates. (**A**) Evolution of the overlap area with time, $S(t)/S_0$, due to the Casimir self-alignment at two distinct equilibrium distances, L_{eq} = 160 nm and L_{eq} = 110 nm. The Au seed size is 7 μm in both cases. Insets depict exemplary video frames corresponding to data points marked on the $S(t)/S_0$ graph. (**B**) Evolution of lateral displacement between the centers of mass of the floating flake and the seed with time, $x(t)$, for the dimers shown in (A), eventually leading to a complete overlap, i.e., $x = 0$, in both cases. Black curves are exponential fits of the experimental displacement data. (**C**) Evolution of the overlap area between the seed and Au flake with time, $S(t)/S_0$, marking distinct phases of lateral and rotational motions for an L_{eq} = 118 nm dimer. The Au seed size is 7 μm. Insets depict exemplary video frames corresponding to data points marked on the $S(t)/S_0$ graph. (**D**) Evolution of angle between the seed's and the floating flake's edges with time, $\theta(t)$, illustrating the self-alignment process. Black line marks an exponential fit of the experimental alignment data.

are distance-independent constants of the electrostatic and Casimir potentials, κ^{-1} is the Debye-Hückel screening length, and $\alpha \approx 2.6$ is the Casimir potential power law for 30-nm-thick Au flakes (*25*). On the contrary, the lateral diffusion coefficient decreases with a decrease in L_{eq} as $D_x \sim L_{eq}^{\beta}$. However, according to previous hydrodynamic simulations, it exhibits a slower dependence with distance, with $\beta < 1$ (*31*). Consequently, the effective frequency $\tilde{\omega}$ is expected to increase with a decrease in L_{eq}, so the lateral motion occurs faster when L_{eq} is smaller, as illustrated by the exponential fits depicted in Fig. 2B (the fitting procedure is described in Methods).

In Fig. 2C, we use the same method as in Fig. 2A but for a different dimer configuration. As depicted in the plot, lateral motion plays a dominant role until ≈7 s mark, at which point the floating flake is found exactly on top of the seed but with an opposing orientation ($\theta \approx 60°$). From that point on, the rotational motion becomes dominant, causing the floating flake to rotate around the vertical axis under the influence of the Casimir torque until it achieves full alignment (see movie S3). Since the lateral motion becomes negligible after the first 7 s, we find it reasonable to analyze solely rotational motion by tracking changes in $\theta(t)$ over time, as depicted in Fig. 2D. Similar to the lateral displacements, this rotational motion conforms to decaying exponential function with an effective ~1 Hz frequency (see Supplementary Theory and Methods), starting from a state of complete misalignment ($\theta \approx 60°$) and culminating in a state of perfect alignment ($\theta = 0°$). It is worth mentioning that in general, the lateral and rotational motions are coupled and in most cases occur simultaneously, creating a system that is too complex to analyze (see fig. S8). However, in a few particular cases (such as the ones illustrated in Figs. 1 and 2), we observed the two motions in a nearly isolated fashion, which allowed for their independent analysis.

Thus, our method results in the precise positioning (trapping) of floating Au flakes within three-dimensional space, offering control over their vertical, horizontal, and rotational orientations. This unique quantum trapping approach harnesses quantum vacuum fluctuations,

rather than real fields (as in, e.g., optical tweezing), for particle manipulation (*21*, *25*). Despite the inherent influence of thermal fluctuations, the trapping potential created by the Casimir effect exhibits stability, enabling controlled particle confinement. In the subsequent sections, we delve into an in-depth investigation of thermal fluctuations, specifically focusing on their magnitude and the resulting particle displacement, especially concerning rotational motion around the vertical axis.

Calculation of the lateral and rotational Casimir effect between two triangular flakes

To improve our understanding of the observed phenomenon and confirm its primary association with the Casimir effect, we conducted both analytical and numerical computations focusing on the in-plane motion of flat triangular Au flakes induced by vacuum fluctuations. The analytical calculations were performed using the Lifshitz formalism (*4*, *5*) and involved several critical approximations to model the underlying dynamics.

First, the Casimir-Lifshitz potential U_{Lif} per unit area for the system comprising two identical infinite Au planar mirrors immersed in an aqueous solution and separated by a gap of thickness L was calculated using the following expression

$$U_{\mathrm{Lif}}(L)=\frac{\hbar c}{4\pi^2}\int_0^\infty \mathrm{d}\xi \int_0^\infty k_\parallel \mathrm{d}k_\parallel \sum_{\mathrm{p,s}} \ln\left[1-r_{\mathrm{p,s}}^2(i\xi,k_\parallel,d_{\mathrm{Au}})e^{-2L\sqrt{k_\parallel{}^2+\xi^2\varepsilon_{\mathrm{H_2O}}(i\xi)}}\right] \tag{1}$$

where the integration was performed over the imaginary frequencies $\xi = i\omega/c$, normalized by the speed of light c, and the wave vector components along the mirrors $k_\parallel$. The summation involved both p- and s-polarizations. Here, $r_{\mathrm{p,s}}(i\xi, k_\parallel, d_{\mathrm{Au}})$ are the Fresnel reflection coefficients for the gold plates evaluated at various wave vectors, polarizations, and mirror thicknesses d_{Au}. The dielectric functions of gold $\varepsilon_{\mathrm{Au}}(i\xi)$ and water $\varepsilon_{\mathrm{H2O}}(i\xi)$ were evaluated at the imaginary frequencies.

Second, to account for the shape and size of the floating flakes and seeds, we used the overlap approximation. This approximation assumes that the Casimir-Lifshitz potential is proportional to the overlap area between the flake and the seed while neglecting any edge effects. In this approach, the lateral potential can be expressed as follows

$$E_{\mathrm{lat}}(x,y,\theta)\approx S(x,y,\theta)U_{\mathrm{Lif}}(L_{\mathrm{eq}}) \tag{2}$$

where x and y are the in-plane displacements, θ is the in-plane rotation angle, $S(x, y, \theta)$ is the overlap area between the flake and the seed, and U_{Lif} is the Casimir-Lifshitz potential per unit area evaluated at L_{eq}.

Third, we assume that the lateral displacements (along x or y) and rotations (around z by angle θ) are independent of each other, allowing for factorization. Certainly, this assumption is valid only in some particular cases, e.g., the ones analyzed in Figs. 1 and 2. In general, lateral and rotational motions are not independent and require more involved numerical simulations, as discussed below. In the independent scenario, however, we arrive at simplified forms for the potentials: $E_x(x)\approx S(x)U_{\mathrm{Lif}}(L_{\mathrm{eq}})$ for lateral displacement (along x) of perfectly aligned triangles and $E_\theta(\theta)\approx S(\theta)U_{\mathrm{Lif}}(L_{\mathrm{eq}})$ for rotation of triangles with the same position of the center of mass. In our experiments, we focused on equilateral triangles, where the corresponding overlap areas are expressed as follows

$$S(x)|_{\theta=0}=S_0\left(\frac{a-x}{a}\right)^2,\quad S(\theta)|_{x=0}=S_0\frac{\mathrm{tg}(\pi/3-\theta/2)-\mathrm{tg}(\theta/2)}{\sqrt{3}} \tag{3}$$

where S_0 is the area of an equilateral triangle with the edge a. Lateral Casimir forces and Casimir torques can be obtained by differentiating E_x and E_θ, correspondingly, along their respective motions (see Supplementary Theory).

To assess the significance of the edge effects, we conducted a comparative analysis between the analytical calculations within the overlap approximation and numerical simulations using the code SCUFF-EM (*42*, *43*). Specifically, we simulated the relative rotation and in-plane translation of two vertically trapped Au equilateral triangles immersed in an aqueous solution, where the Casimir and electrostatic forces at L_{eq} are balanced. Figure 3 presents the simulation results alongside analytical calculations. Because of the symmetry of the equilateral triangles, we considered rotation angles ranging from 0° to 60°. Examining the rotational dependence of the Casimir energy normalized to the corresponding triangle surface area at zero x and y displacements, it is evident that the numerical curve approaches the analytical approximation as the triangle size increases. For triangles with $a \sim 8$ μm, the overlap approximation performs exceptionally well for $\theta > 10°$ (Fig. 3A). As mentioned earlier and detailed in Supplementary Theory, the lateral Casimir potential has a nonharmonic shape in the overlap approximation. However, at small angles, the edge effects captured by SCUFF-EM simulations become prominent, resulting in a quasi-harmonic potential, as shown in Fig. 3A (see also Supplementary Theory and figs. S6 and S7). This effect is even more pronounced for the Casimir torque, normalized to the overlap area $S(\theta,0)$ (Fig. 3B). Here, the overlap approximation performs well at $\sim\theta > 20°$. However, at small angles, the edge effects become considerable. The torque cannot surpass the limit set by the overlap approximation at any angle. Furthermore, the torque reaches its maximum at an angle where an optimal balance between edge effects and increased overlap area is attained. With increasing triangle size, the role of edge effects diminishes, causing the optimal angle to decrease, and eventually approach zero for infinite triangles. Notably, unlike the anisotropic finite-sized systems considered by Antezza *et al.* (*17*), we observe high accuracy of the overlap approximation for large triangles owing to their isotropy.

For nonzero in-plane displacements of the triangles, the discussed phenomena become even more intricate. Figure 3 (C and D) shows the combined influence of translation and rotation on the Casimir energy and torque, respectively. The energy's dependence on displacements consistently reaches a minimum in the center at $x = y = 0$ (Fig. 3C), corresponding to the stable configuration of the system and the lateral Casimir trapping. As rotation is introduced ($\theta \neq 0$), the energy colormap undergoes a shape transition from hexagon to triangle forms, although this does not lead to qualitative changes. The role of rotation is evident in the torque colormaps (Fig. 3D). For a nonzero rotation angle, in the region of zero displacements, a pronounced spot of maximum torque emerges, aligning with the earlier discussed scenario of rotation at zero displacements. Even at zero rotation, the interplay between the system's geometry and relative displacements may lead to nonvanishing torques. This effect disappears on the symmetry axes of the rotated triangle, having different signs on opposite sides of these axes. In addition, at $\theta = 60°$, the rotated system becomes so symmetric that the torque is entirely compensated in the large area around zero displacements. For all intermediate angles (additional data shown in the Supplementary Materials) between 0° and

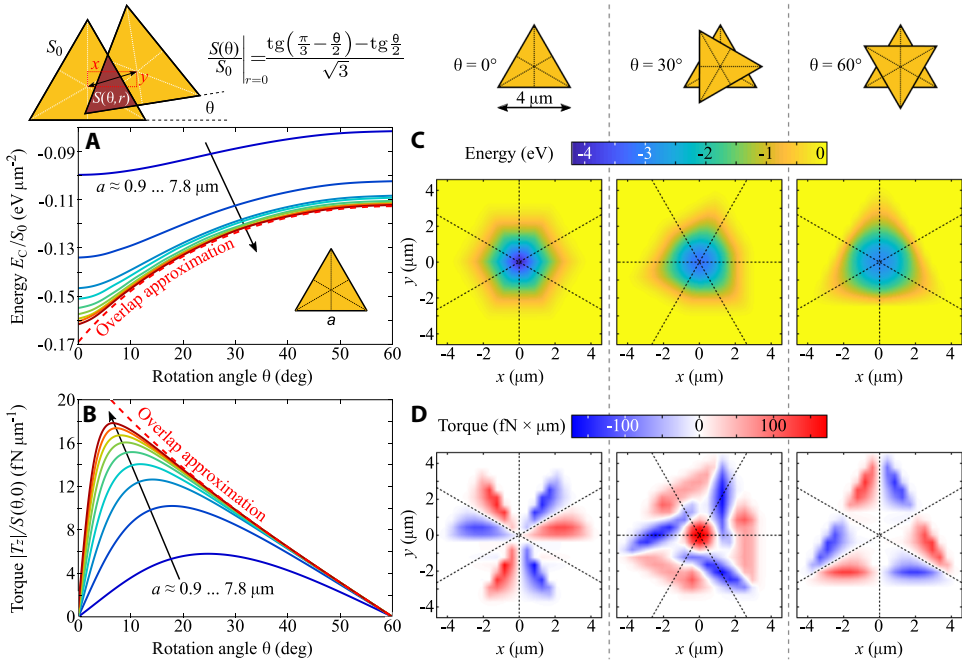

Fig. 3. Calculation of the lateral Casimir interactions of two gold equilateral triangles. The triangles that have edge a, thickness 40 nm, and surface area S_0 are vertically trapped at $L_{eq} = 200$ nm and immersed in aqueous solution, for the relative rotation by angle θ and/or translation by $r = (x, y)$. (**A**) Casimir energy versus the rotation angle of one triangle around the center of mass. The energy normalized to triangle surface area S_0 increases with size until the limit determined by the overlap area, $S(\theta, r = 0)$, of two mutually rotated triangles. (**B**) Casimir torque T_z around an axis normal to the triangle surface and going through the center of mass normalized to the overlap area $S(\theta, 0)$ versus θ, exhibiting an asymmetric increase toward small angles. (**C** and **D**) Casimir energy and torque for two triangles ($a = 4$ µm) as a function of both rotation around the center of mass (θ = 0°, 30°, and 60°) and translation (x, y). The dashed lines mark the symmetry axes of therotated triangle.

60°, a mixed pattern emerges, with maximum torque at the center, surrounded by areas of effective torque induced by displacements and rotations. These areas deviate from the symmetry axes of the rotated triangle but maintain alternating torque signs around the central maximum. Consequently, as the flake moves with simultaneous displacement and rotation, additional torque in the opposing direction may arise, resulting in a crawling-like motion.

Impact of equilibrium distance, seed area, and thermal fluctuations on stability of Casimir self-alignment

The self-alignment experiments are conducted in the L_{eq} range spanning ~100 to 200 nm, where conditions allow establishing a stable equilibrium and a sufficiently deep trapping potential. In each self-alignment measurement, L_{eq} is precisely determined by assessing the reflection spectrum of the stable FP microcavity, Fig. 1F, and subsequently fitting the spectrum using the transfer-matrix method (see Methods).

To investigate the impact of L_{eq} on self-alignment, we maintain a fixed seed size, $a = 4$ µm, while choosing a floating flake that matches this seed size. Optical tweezers are used to bring the flake into close proximity with the seed and then allow it to freely diffuse until the Casimir potential ensures the formation of a stable dimer. Subsequently, we track the dynamics of the angle between the triangles over time, θ(t). When θ = 0, the floating Au flake perfectly aligns with the seed, and the Casimir potential is minimized, thus corresponding to the equilibrium position, as illustrated in Fig. 3A.

Figure 4 (A to D) illustrates the variations in θ(t) for four distinct L_{eq} values: 195, 180, 138, and 114 nm, respectively, as a result of thermal fluctuations. Specifically, in Fig. 4A, the fluctuations in θ are the strongest among situations presented in Fig. 4. This is attributed to the fact that at this L_{eq}, the thermal energy (k_BT) approaches the depth of the trapping potential, leading to more pronounced deviations in θ(t) from its equilibrium position due to thermal fluctuations. As a result, the floating flake exhibits fluctuations of up to ±20° at different points in time [see θ distributions and standard deviations (SDs) to the right of the corresponding θ(t) plots].

The fluctuations of θ decrease upon reduction in L_{eq}. To demonstrate that, we fit the experimental histograms of θ(t) to the normal distribution functions and find that the variances, denoted as σ_θ, grow with L_{eq}, as depicted in Fig. 4E. The reason for this lies in the steep dependence of the trapping Casimir potential on the distance, $U_C \propto L_{eq}^{-2.6}$ (*25*) as discussed above. Furthermore, we determine σ_θ theoretically by substituting the analytical Casimir-Lifshitz potential from Eq. 1 into the equation for the mean square displacement using Gibbs formalism (see Methods, Eq. 5). Combined with the overlap approximation and the Casimir potential from SCUFF-EM simulations, we arrive at results that are qualitatively similar to experimental observations. Our theoretical results are especially close to the experimental findings at small L_{eq}; however, they underestimate σ_θ approximately twofold (for SCUFF-EM simulations) at large L_{eq}. This discrepancy can be attributed to electrostatics, which was not included in our calculations and modeling, given its relatively weak contribution compared to Casimir forces. The relative contribution of the electrostatic part to the total potential increases with L_{eq}, contributing to the growing mismatch at large separations. Furthermore,

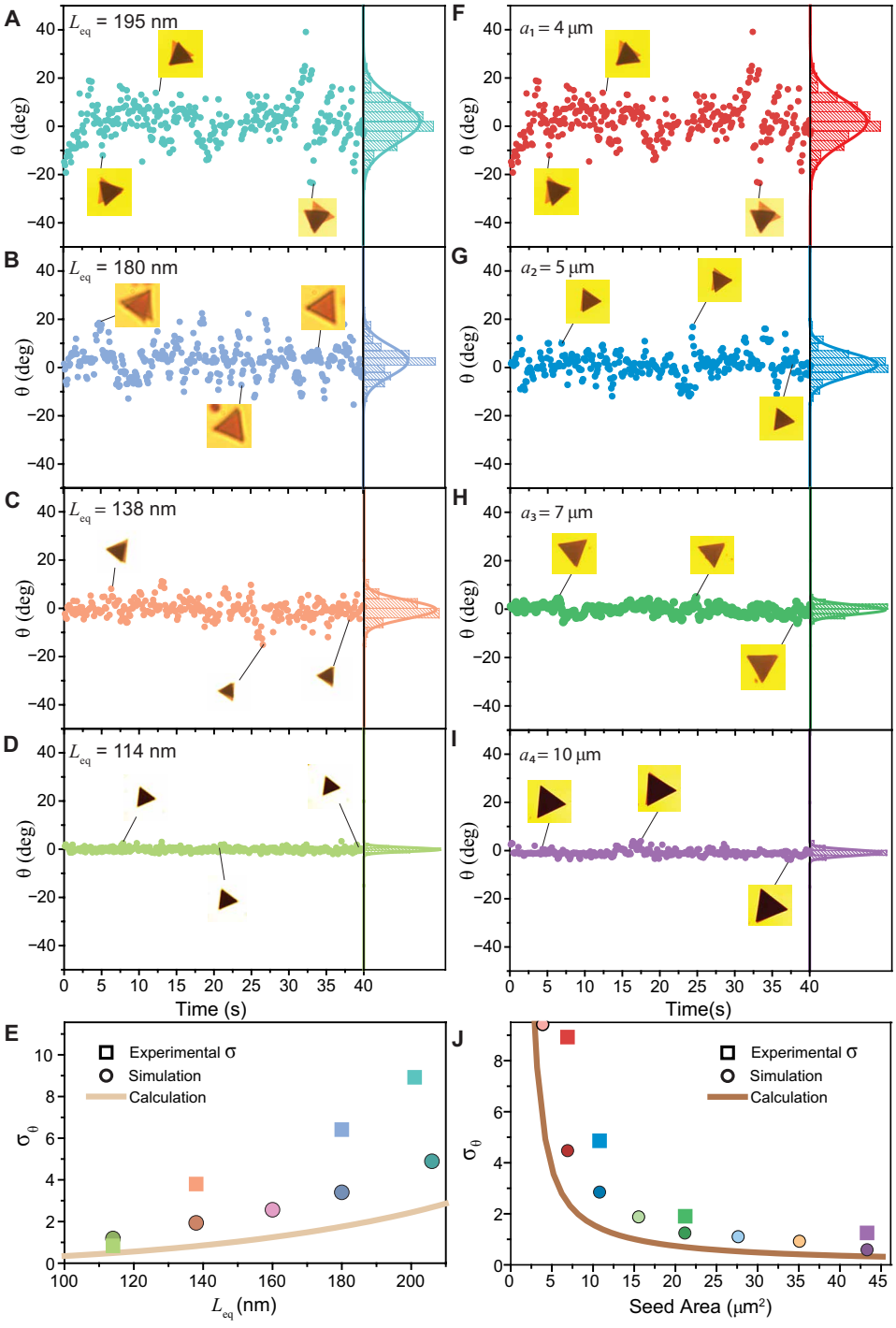

Fig. 4. Impact of equilibrium distance and flake's area on stability of self-alignment to thermal fluctuations. Variation of angle θ(*t*) in time for stable dimers of $a = 4$ μm seed and a floating flake of similar size for $L_{eq} = 195$ nm (**A**), $L_{eq} = 180$ nm (**B**), $L_{eq} = 138$ nm (**C**), and $L_{eq} = 114$ nm (**D**). The distributions of θ are shown on the right of the corresponding time traces and are fitted to a normal distribution. Insets depict exemplary video frames corresponding to data points on the graph. (**E**) SD (σ_θ) versus L_{eq}. Variation of angle θ(*t*) in time for stable dimers at $L_{eq} \approx 195$ nm and seeds with lateral sizes of 4 (**F**), 5 (**G**), 7 (**H**), and 10 μm (**I**). In all cases, the sizes of floating flakes were approximately the same as the corresponding seeds. The normal distribution of the θ is shown on the right side of each panel. Insets images indicate the video frames to the corresponding data points on the graph. (**J**) SD, σ_θ, for various Au seed areas. In (E) and (J), the simulation points are obtained using SCUFF-EM and the calculation curves, with the Lifshitz formalism in the overlap approximation.

the difference between the analytical and numerical results reflects the significance of the edge effects, especially at small deviations from equilibrium. In addition, the accuracy of the overlap approximation not only increases with the size of the flakes (a), as we discussed earlier, but also with a decrease in L_{eq}. In other words, the analytical approximation's accuracy increases with the ratio a/L_{eq}. Last, it is important to note that at small displacements (x and y), the Casimir torques [and hence $\theta(t)$] are almost independent of displacements (see Fig. 3D), justifying our analysis.

The magnitude of the trapping potential scales with the area overlap of the seed and the floating Au flake. This is a fundamental reason for the rotational self-alignment observation in the seed configuration; Au flakes in the aqueous solution strive to maximize their overlap areas with the seeds due to strong Casimir attraction. As previously, we preselect the flakes such that they match the shape and size of the corresponding seed, which simplifies experiments and allows for precise tracking of the rotational motion of the floating flake $\theta(t)$ (see movie S4).

In the subsequent study, we probe the stability of the trapping potential to thermal fluctuations for a fixed $L_{eq} \approx 195$ nm, as a function of the total area of the seed, S_0 (Fig. 1B). We specifically investigate four different seed sizes in the range between 4 and 10 μm, depicted in Fig. 4 (F to I). As expected from the Casimir energy calculations (see Fig. 3A), increasing the area of Au seeds increases the Casimir energy (and the depth of the trapping potential), which results in more stable microcavities.

The stability dependence on the overlap area is shown in Fig. 4 (F to I) by plotting the dynamics of $\theta(t)$ caused by thermal fluctuations for $a = 4$, 5, 7, and 10 μm triangle seed sizes. The SDs, σ_θ, obtained from fits of $\theta(t)$ histograms to the normal distribution function, indicate that the stability strongly depends on the area overlap. In particular, the biggest flakes display the most pronounced stability, i.e., the stability is inversely proportional to the flake area, or more accurately, $\sigma_\theta \propto S_0^{-1.2}$ (Fig. 4J). This aligns with the analytical calculations and numerical simulations discussed in the previous paragraphs. However, in this case, the difference between the calculations and measurements remains consistent across different overlap areas. This further validates that the discrepancy is caused by the contribution of the electrostatic potential. These results demonstrate that control of lateral stability of the FP cavity can be achieved by selecting various seed sizes while maintaining the same separation distance (see movie S5).

Last, we note that the stability of the self-alignment process is not notably affected by the Au flake (or seed) thickness within the range of 20 to 35 nm used in our experiments. The resulting variance of the Casimir potential is less than 5% (see fig. S9, where we present a theoretical calculation based on Lifshitz formalism).

In conclusion, vertically and laterally stable self-assembled and rotationally self-aligned Casimir microcavities can be formed by equilibrating two opposing forces: attractive Casimir and repulsive electrostatic. The so-formed microcavities exhibit optical FP resonances in the visible spectral range, observed as pronounced reflection colors. Control of the self-alignment of the cavity is demonstrated by using triangular templated substrates and is studied upon variation of two independent parameters: (i) the equilibrium distance, L_{eq}, between the floating flake and the templated substrate, and (ii) the flake area, S_0, by varying the seed and the floating flake sizes. These two parameters are straightforward to control; therefore, our method offers flexibility to achieve the desired conditions for liquid-phase Casimir torque experiments. Furthermore, we investigated the stability of self-alignment to thermal fluctuations, which was assessed by examining $\theta(t)$ as a function of L_{eq} and S_0. We find that our experimental observations are in good agreement with Casimir-Lifshitz theory and with SCUFF-EM numerical modeling. This work presents a self-assembly and self-alignment platform based on quantum trapping and templated substrates that is suitable for Casimir torque experiments. Furthermore, the presented FP microcavities are stable at room temperature for as long as they have been monitored, which offers a possibility of their future use in nanomachinery (*21*), self-assembly (*28*), optomechanics (*44*), polaritonic chemistry (*45*), and other potential cavity-inspired applications (*46*–*48*).

METHODS

Seed fabrication

All seed samples were prepared on thin (170 μm) microscope glass coverslips. The glass coverslips were cleaned in acetone, 2-propanol, and water at 50°C in an ultrasonicator for 15 min for each solvent. Subsequently, the coverslips were dried using compressed nitrogen, followed by oxygen plasma cleaning. Triangular Au seed arrays with various edge sizes were fabricated using standard electron-beam lithography (Raith EBPG 5200). To provide the adhesion of the Au to the glass substrate, first, a 2-nm Cr layer was evaporated. Subsequently, a 20-nm Au layer was evaporated. Both layers were evaporated using the Kurt J. Lesker PVD 225 tool.

Gold flake synthesis and KBr preparation

Single-crystal Au flakes were synthesized using an aniline-assisted method in ethylene glycol (EG) (*41*). This synthesis method is preferred because of its ability to produce colloidal microflakes with a large aspect ratio between their lateral size and thickness. In brief, the synthesis protocol includes the following steps. First, a 0.72 mM $HAuCl_4 \cdot 3H_2O$ solution in 50 ml of EG is prepared in a glass bottle and heated to 95°C in a water bath for 20 min. Second, a 0.1 M aniline solution in EG is added to the heated solution under mild stirring until the molar ratio reaches 2:1 of aniline to gold. To reach this molar ratio, a 0.72 ml of 0.1 M aniline is added in our case, since our initial solution contained a 50 ml of 0.72 mM $HAuCl_4 \cdot 3H_2O$. When the aniline is mixed homogeneously, the reaction is kept undisturbed in a water bath at 95°C for 3 hours. This synthesis protocol yields Au flakes with a high aspect ratio, with flake thicknesses ranging from 20 to 35 nm and lateral dimensions varying from 3 to 15 μm. After successful synthesis, the solution contains a large number of precipitated Au flakes on the bottom or walls of the bottle. In addition, the synthesis yields a large amount of by-product, quasi-spherical Au particles in the solution. Therefore, it is important to remove the spherical particles and to replace the EG with cetyltrimethylammonium bromide (CTAB) aqueous solution. This replacement requires several steps of washing. Specifically, after the Au flakes sediment, half of the volume of the supernatant is removed and replaced with the same volume of pure 20 mM CTAB aqueous solution. The new mixture is shaken to disperse the CTAB and form a double layer on the surface of the Au flakes. This step is repeated several times until most of the spherical particles are removed and EG is replaced with the 20 mM CTAB solution. Once the replacement of EG is completed, the CTAB concentration in the solution is further diluted to the 1 mM level. The final synthesis batch is stored at this CTAB concentration for subsequent use. In self-alignment experiments, the CTAB concentration was

further diluted to 0.1 mM and the final ionic environment was adjusted with an aqueous solution of potassium bromide (KBr). To do that, KBr salt is dissolved in deionized water in the desired concentration and subsequently mixed with the 0.1 mM CTAB. The total ion concentration in solution is a parameter that is directly connected to the Debye-Hückel screening length, defined as

$$\kappa^{-1} = \sqrt{\frac{\varepsilon_{H_2O}(0)\varepsilon_0 k_B T}{C_{tot} q_0^2 z^2}} \quad (4)$$

where $\varepsilon_{H2O}(0)$ is the static permittivity of water, ε_0 is the vacuum permittivity, q_0 is the elementary charge, C_{tot} is the total ion concentration with valence z (in this case, ions are CTA^+ and Br^- from CTAB and K^+ and Br^- from salt; therefore, $z = 1$ in all cases).

Optical measurements

All reflectivity and self-alignment measurements were performed using an inverted microscope (Nikon Eclipse TE2000-E) equipped with an oil immersion 100× objective with an adjustable numerical aperture (NA = 0.5 to 1.3). All reflection spectra are taken at quasi-normal incidence using NA = 0.5 and a halogen light source, and the reflected spectrum is directed to the fiber-coupled spectrometer (Andor, Shamrock 500i), equipped with a charge-coupled device camera (Andor, Newton 920). The equilibrium distance, L_{eq}, was assessed by fitting the experimentally measured reflectivity spectra with the transfer-matrix method (see figs. S1 to S3).

For the selection of the Au flakes with the correct size and shape, the optical tweezers method was used. To trap the Au flakes, a λ = 447 nm continuous-wave laser with a power of 9 mW was focused on the desired flake through a 100× objective (NA = 1.3). All self-alignment data are collected through recording videos using a Thorlabs DCC1645C-HQ camera and each video frame is analyzed using MATLAB, allowing to extract the dynamics of angle, $\theta(t)$, for subsequent analysis of the Casimir self-alignment process.

Fitting procedure

To fit the experimental observations of lateral and rotational microcavity formation observed in Fig. 2, we used the decaying exponential solution described in detail in the Supplementary Theory. The expression for the lateral motion reads: $x(t) = \tilde{a}[1 - e^{\tilde{\omega}(t-t_{max})}]$, where $\tilde{a} = a(1 - e^{-\tilde{\omega}t_{max}})^{-1}$ and a is the triangle's edge size. The fitting parameters for the lateral motion shown in Fig. 2B are as follows: $\tilde{a}_{160} = 6.2$ μm, $\tilde{\omega}_{160} = 0.25\,s^{-1}$, and $t_{max} = 10.3$ s for $L_{eq} = 160$ nm cavity; and $\tilde{a}_{110} = 7.7$ μm, $\tilde{\omega}_{110} = 0.33\,s^{-1}$, and $t_{max} = 11.7$ s, for $L_{eq} =$ 110 nm cavity, respectively. For rotational motion, shown in Fig. 2D, we similarly use $\theta(t) = \tilde{\theta}_0[1 - e^{\tilde{\omega}(t-t_{max})}]$, where $\tilde{\theta}_0 = \theta_0(1 - e^{-\tilde{\omega}t_{max}})^{-1}$ and $\theta_0 = 60°$. The extracted parameters are: $\tilde{\theta}_0 = 66°$, $\tilde{\omega} = 0.7\,s^{-1}$, and $t_{max} = 3.5$ s.

Calculations of the angular spread

To theoretically determine the SD of angle θ describing rotations under the lateral Casimir potential $E(\theta)$ and subjected to thermal fluctuations at temperature T, we used the expression for the mean squared displacement in Gibbs formalism

$$\sigma_\theta = \sqrt{\langle\theta^2\rangle} = \sqrt{\int_{-60°}^{60°} \theta^2 e^{-E(\theta)/k_B T} d\theta \Big/ \int_{-60°}^{60°} e^{-E(\theta)/k_B T} d\theta} \quad (5)$$

where we account for the symmetry of the potential, implying $\langle\theta\rangle = 0$. Substituting the analytical Casimir-Lifshitz potential from Eq. 1, combined with the overlap approximation $E(\theta) \approx S(\theta)U_{Lif}(L_{eq})$ and the Casimir potential from the SCUFF-EM simulations, we obtained the final results denoted as calculations and simulations, respectively, in Fig. 4.

Supplementary Materials

This PDF file includes:

Figs. S1 to S9
Note S1
Legends for movies S1 to S5
Supplementary Theory

Other Supplementary Material for this manuscript includes the following:

Movies S1 to S5

REFERENCES AND NOTES

1. F. London, The general theory of molecular forces. *Trans. Faraday Soc.* **33**, 8b–26b (1937).
2. H. B. G. Casimir, D. Polder, The influence of retardation on the London-van der Waals forces. *Phys. Rev.* **73**, 360–372 (1948).
3. H. B. G. Casimir, On the attraction between two perfectly conducting plates. *Proc. Kon. Ned. Akad. Wet.* **B51**, 793–795 (1948).
4. E. M. Lifshitz, The theory of molecular attractive forces between solids. *Sov. Phys. JETP* **2**, 73–83 (1956).
5. I. E. Dzyaloshinskii, E. M. Lifshitz, L. P. Pitaevskii, The general theory of van der Waals forces. *Adv. Phys.* **10**, 165–209 (1961).
6. J. Munday, F. Capasso, V. Parsegian, Measured long-range repulsive Casimir–Lifshitz forces. *Nature* **457**, 170–173 (2009).
7. J. N. Munday, F. Capasso, Repulsive Casimir and van der Waals forces: From measurements to future technologies. *Int. J. Mod. Phys. A* **25**, 2252–2259 (2010).
8. F. Chen, U. Mohideen, G. L. Klimchitskaya, V. M. Mostepanenko, Demonstration of the lateral Casimir force. *Phys. Rev. Lett.* **88**, 101801 (2002).
9. F. Chen, U. Mohideen, G. L. Klimchitskaya, V. M. Mostepanenko, Experimental and theoretical investigation of the lateral Casimir force between corrugated surfaces. *Phys. Rev. A* **66**, 032113 (2002).
10. R. B. Rodrigues, P. A. Maia Neto, A. Lambrecht, S. Reynaud, Lateral Casimir force beyond the proximity-force approximation. *Phys. Rev. Lett.* **96**, 100402 (2006).
11. E. I. Kats, Van der Waals forces in non-isotropic systems. *Sov. Phys. JETP* **33**, 634 (1971).
12. V. A. Parsegian, G. H. Weiss, Dielectric anisotropy and the van der Waals interaction between bulk media. *J. Adhes.* **3**, 259–267 (1972).
13. Y. S. Barash, Moment of van der Waals forces between anisotropic bodies. *Radiophys. Quantum Electron.* **21**, 1138–1143 (1978).
14. D. A. T. Somers, J. L. Garrett, K. J. Palm, J. N. Munday, Measurement of the Casimir torque. *Nature* **564**, 386–389 (2018).
15. B. Spreng, T. Gong, J. N. Munday, Recent developments on the Casimir torque. *Int. J. Mod. Phys. A* **37**, 2241011 (2022).
16. R. Guérout, C. Genet, A. Lambrecht, S. Reynaud, Casimir torque between nanostructured plates. *EPL* **111**, 44001 (2015).
17. M. Antezza, H. B. Chan, B. Guizal, V. N. Marachevsky, R. Messina, M. Wang, Giant Casimir torque between rotated gratings and the θ = 0 anomaly. *Phys. Rev. Lett.* **124**, 013903 (2020).
18. Z. Xu, T. Li, Detecting Casimir torque with an optically levitated nanorod. *Phys. Rev. A* **96**, 033843 (2017).
19. J. Ahn, Z. Xu, J. Bang, Y.-H. Deng, T. M. Hoang, Q. Han, R.-M. Ma, T. Li, Optically levitated nanodumbbell torsion balance and GHz nanomechanical rotor. *Phys. Rev. Lett.* **121**, 033603 (2018).
20. J. Ahn, Z. Xu, J. Bang, P. Ju, X. Gao, T. Li, Ultrasensitive torque detection with an optically levitated nanorotor. *Nat. Nanotechnol.* **15**, 89–93 (2020).
21. R. Zhao, L. Li, S. Yang, W. Bao, Y. Xia, P. Ashby, Y. Wang, X. Zhang, Stable Casimir equilibria and quantum trapping. *Science* **364**, 984–987 (2019).
22. B. V. Derjaguin, L. D. Landau, Theory of the stability of strongly charged lyophobic sols and of the adhesion of strongly charged particles in solutions of electrolytes. *Acta Physicochim. U.R.S.S.* **14**, 633–662 (1941).
23. E. J. W. Verwey, Theory of the stability of lyophobic colloids. *J. Phys. Colloid. Chem.* **51**, 631–636 (1947).
24. S. Biggs, P. Mulvaney, Measurement of the forces between gold surfaces in water by atomic force microscopy. *J. Chem. Phys.* **100**, 8501–8505 (1994).

25. B. Munkhbat, A. Canales, B. Küçüköz, D. G. Baranov, T. O. Shegai, Tunable self-assembled Casimir microcavities and polaritons. *Nature* **597**, 214–219 (2021).
26. G. M. Whitesides, B. Grzybowski, Self-assembly at all scales. *Science* **295**, 2418–2421 (2002).
27. Y. K. Cho, R. Wartena, S. M. Tobias, Y.-M. Chiang, Self-assembling colloidal-scale devices: Selecting and using short-range surface forces between conductive solids. *Adv. Func. Mater.* **17**, 379–389 (2007).
28. C. A. Silvera Batista, R. G. Larson, N. A. Kotov, Nonadditivity of nanoparticle interactions. *Science* **350**, 1242477 (2015).
29. V. Esteso, S. Carretero-Palacios, H. Míguez, Casimir–Lifshitz force based optical resonators. *J. Phys. Chem. Lett.* **10**, 5856–5860 (2019).
30. L. Ge, X. Shi, Z. Xu, K. Gong, Tunable Casimir equilibria with phase change materials: From quantum trapping to its release. *Phys. Rev. B* **101**, 104107 (2020).
31. F. Schmidt, A. Callegari, A. Daddi-Moussa-Ider, B. Munkhbat, R. Verre, T. Shegai, M. Käll, H. Löwen, A. Gambassi, G. Volpe, Tunable critical Casimir forces counteract Casimir–Lifshitz attraction. *Nat. Phys.* **19**, 271–278 (2023).
32. M. Rycenga, P. H. C. Camargo, Y. Xia, Template-assisted self-assembly: A versatile approach to complex micro- and nanostructures. *Soft Matter* **5**, 1129–1136 (2009).
33. Y. Zhou, X. Zhou, D. J. Park, K. Torabi, K. A. Brown, M. R. Jones, C. Zhang, G. C. Schatz, C. A. Mirkin, Shape-selective deposition and assembly of anisotropic nanoparticles. *Nano Lett.* **14**, 2157–2161 (2014).
34. C. Hanske, M. Tebbe, C. Kuttner, V. Bieber, V. V. Tsukruk, M. Chanana, T. A. F. König, A. Fery, Strongly coupled plasmonic modes on macroscopic areas via template-assisted colloidal self-assembly. *Nano Lett.* **14**, 6863–6871 (2014).
35. L. Scarabelli, D. Vila-Liarte, A. Mihi, L. M. Liz-Marzán, Templated colloidal self-assembly for lattice plasmon engineering. *Acc. Mater. Res.* **2**, 816–827 (2021).
36. H. B. Chan, V. A. Aksyuk, R. N. Kleiman, D. J. Bishop, F. Capasso, Quantum mechanical actuation of microelectromechanical systems by the Casimir force. *Science* **291**, 1941–1944 (2001).
37. S. Sanders, W. J. M. Kort-Kamp, D. A. R. Dalvit, A. Manjavacas, Nanoscale transfer of angular momentum mediated by the Casimir torque. *Commun. Phys.* **2**, 71 (2019).
38. A. Ashourvan, M. F. Miri, R. Golestanian, Noncontact rack and pinion powered by the lateral Casimir force. *Phys. Rev. Lett.* **98**, 140801 (2007).
39. F. C. Lombardo, F. D. Mazzitelli, P. I. Villar, Exploring the quantum vacuum with cylinders. *J Phys. A Math. Theor.* **41**, 164009 (2008).
40. I. Cavero-Peláez, K. A. Milton, P. Parashar, K. V. Shajesh, Noncontact gears. II. Casimir torque between concentric corrugated cylinders for the scalar case. *Phys. Rev. D* **78**, 065019 (2008).
41. Z. Guo, Y. Zhang, Y. DuanMu, L. Xu, S. Xie, N. Gu, Facile synthesis of micrometer-sized gold nanoplates through an aniline-assisted route in ethylene glycol solution. *Colloids Surf. A Physicochem. Eng. Asp.* **278**, 33–38 (2006).
42. M. T. Homer Reid, A. W. Rodriguez, J. White, S. G. Johnson, Efficient computation of Casimir interactions between arbitrary 3D objects. *Phys. Rev. Lett.* **103**, 040401 (2009).
43. https://github.com/HomerReid/scuff-em. Accessed: 2024-02-13. Surface-CUrrent-Field Formulation of ElectroMagnetism (SCUFF-EM).
44. M. Eichenfield, R. Camacho, J. Chan, K. J. Vahala, O. Painter, A picogram-and nanometre-scale photonic-crystal optomechanical cavity. *Nature* **459**, 550–555 (2009).
45. A. Thomas, L. Lethuillier-Karl, K. Nagarajan, R. M. A. Vergauwe, J. George, T. Chervy, A. Shalabney, E. Devaux, C. Genet, J. Moran, T. W. Ebbesen, Tilting a ground-state reactivity landscape by vibrational strong coupling. *Science* **363**, 615–619 (2019).
46. P. Törmä, W. L. Barnes, Strong coupling between surface plasmon polaritons and emitters: A review. *Rep. Prog. Phys.* **78**, 013901 (2014).
47. D. G. Baranov, M. Wersäll, J. Cuadra, T. J. Antosiewicz, T. Shegai, Novel nanostructures and materials for strong light-matter interactions. *ACS Photonics* **5**, 24–42 (2018).
48. F. J. Garcia-Vidal, C. Ciuti, T. W. Ebbesen, Manipulating matter by strong coupling to vacuum fields. *Science* **373**, eabd0336 (2021).

Acknowledgments

Funding: We acknowledge financial support from the Swedish Research Council (VR Miljö project, grant no. 2016-06059; VR project, grant no. 2017-04545; and VR project, grant no. 2022-03347), the Knut and Alice Wallenberg Foundation (grant no. 2019.0140), Chalmers Area of Advance Nano, 2D-TECH VINNOVA competence center (ref. 2019-00068), and Olle Engkvists foundation (grant no. 211-0063). T.J.A. acknowledges support from the Polish National Science Center via the project 2019/34/E/ST3/00359. The computations were enabled by resources provided by the Swedish National Infrastructure for Computing (SNIC) at PDC and by the Interdisciplinary Centre for Mathematical and Computational Modelling at the University of Warsaw (grant no. G55-6). **Author contributions:** B.K., O.V.K., and T.O.S. conceived the idea and planned the project. B.K. performed all experiments, analyzed the data, and performed TMM fittings. A.C., A.Y.P., and A.V.A. contributed to the nanofabrication of the seed structures. O.V.K. and T.J.A. performed the analytical and numerical calculations. B.K., O.V.K., T.J.A., and T.O.S. wrote the manuscript, with the help of all authors. **Competing interests:** The authors declare that they have no competing interests. **Data and materials availability:** All data needed to evaluate the conclusions in the paper are present in the paper and/or the Supplementary Materials. The raw data can be found at the Zenodo repository using the DOI 10.5281/zenodo.10848097.

Submitted 27 November 2023
Accepted 20 March 2024
Published 24 April 2024
10.1126/sciadv.adn1825